Chemical Geology 312-313 (2012) 58–73

Contents lists available at SciVerse ScienceDirect

Chemical Geology

journal homepage: www.elsevier.com/locate/chemgeo

Research paper

Multi-step TIMS and CA-TIMS monazite U–Pb geochronology

Emily M. Peterman *, James M. Mattinson, Bradley R. Hacker

Department of Earth Science, 1006 Webb Hall, Mail Code 9630, University of California, Santa Barbara, CA 93106-9630, USA

ARTICLE INFO

Article history:
Received 14 July 2011
Received in revised form 5 April 2012
Accepted 9 April 2012
Available online 20 April 2012

Editor: L. Reisberg

Keywords:
Monazite
U–Pb
Geochronology
Chemical abrasion
Annealing

ABSTRACT

Multi-step chemical abrasion thermal ionization mass spectrometry (CA-TIMS) methods were developed for monazite using six samples that vary in composition and age—*Amelia*, *Jefferson County*, *Burke*, *Elk Mountain*, *554* and *Madagascar*. To evaluate whether the multi-step CA-TIMS approach reveals complexities in either age or composition that might be masked by single-step analysis, this study presents a side-by-side comparison of monazite samples dated via multi-step TIMS (not annealed) and CA-TIMS (annealed), and measurement of rare earth element ratios for each dissolution step. The data demonstrate three important contributions. First, annealing reduces solubility—after one partial dissolution step, not-annealed fractions were 3.3–4.1 times more digested than the annealed fractions. The difference in solubility suggests that monazite does not fully self-anneal at low temperatures. Second, multi-step TIMS analyses yielded high-precision U–Pb plateau ages for the *Burke* and *Amelia* monazites; CA-TIMS analyses yielded high-precision U–Pb plateau ages for *Madagascar* and *Amelia* monazites. *Jefferson County*, *Elk Mountain* and *554* yielded more complex results and no U–Pb plateau ages. Third, chemical analysis of partial-dissolution steps reveals heterogeneous age and compositional data for annealed samples. Because not-annealed samples yielded more consistent age and compositional data, high-temperature annealing is not recommended for monazite. Instead, optimal TIMS results are provided by slow, partial dissolution of monazite in weak acid.

1. Introduction

Because determining the rates of large-scale tectonic processes – including exhumation, uplift and burial – remains a fundamental issue in geology, the need for more accurate and precise mineral dates is critical. Geochronologists have long appreciated the potential of monazite [(Ce,Th,REE)PO_4] as a geochronometer for several reasons: 1) it is stable at a wide range of pressures and temperatures over a broad range of bulk compositions (Parrish, 1990; Chang et al., 1998; Catlos et al., 2002; Pyle et al., 2002); 2) it contains U and Th (Overstreet, 1967), thus providing three decay schemes to assess concordance ($^{238}U \rightarrow {}^{206}Pb$, $^{235}U \rightarrow {}^{207}Pb$, $^{232}Th \rightarrow {}^{208}Pb$); 3) it generally contains low initial concentrations of common Pb (Parrish, 1990), thereby reducing the correction for common Pb; 4) and, perhaps most importantly, the low diffusivity of elements within monazite (Cherniak et al., 2004) enables the preservation of compositional zoning that may reflect changes in pressure, temperature, fluid composition, and/or the growth or consumption of other minerals (e.g. Chang et al., 1998; Pyle et al., 2001; Williams et al., 2002; Kohn and Malloy, 2004; Janots et al., 2006). Correlation of monazite composition with mineral reactions and pressure–temperature (*P–T*) histories can provide important pressure–temperature–time (*P–T–t*) information not attainable by other means (e.g. Pyle and Spear, 1999; Dumond et al., 2008; Janots et al., 2009).

A variety of techniques have been used to determine monazite (U–Th)/Pb dates, including laser ablation inductively coupled mass spectrometry (LA-ICPMS), secondary ion mass spectrometry (SIMS), electron probe microanalysis (EPMA) and thermal ionization mass spectrometry (TIMS). Microbeam techniques, including LA-ICPMS, SIMS and EPMA, provide a means to measure in situ dates from monazite; in favorable circumstances, these dates can be used to determine the timing or rates of metamorphic, magmatic and diagenetic processes (Suzuki and Adachi, 1991; Harrison et al., 1995; Stern and Berman, 2001; Foster et al., 2004; Williams et al., 2007). In the simplest terms, LA-ICPMS and SIMS methods measure Pb/U, Pb/Th and the isotopic ratios of Pb in monazite to calculate a date, whereas EPMA methods measure the elemental concentrations of U, Th and Pb to calculate a date.

Several recent improvements in analytical techniques afford smaller microbeam sizes (~5 μm), improved counting accuracy and precision, and shorter analytical times; for example <1 minute total analysis time is now routine via LA-ICPMS (e.g. Gehrels et al., 2008). Unfortunately, the ability to obtain reproducible *and* accurate dates with many of these techniques has proven problematic for several reasons (Horstwood, 2008; Kohn and Vervoort, 2008). First, microbeam techniques require the use of a reference material. The accuracy

* Corresponding author at: Bowdoin College, Earth and Oceanographic Science, 6800 College Station, Brunswick, ME 04011, USA. Tel.: +1 207 725 3846.
E-mail addresses: peterman@bowdoin.edu, emily.peterman@bowdoin.edu (E.M. Peterman), mattinson@geol.ucsb.edu (J.M. Mattinson), hacker@geol.ucsb.edu (B.R. Hacker).

and precision of microbeam dates are therefore limited by instrument reproducibility and the degree of isotopic homogeneity of the reference material—any heterogeneity in the reference material must be incorporated into the errors for an unknown. Second, LA-ICPMS and SIMS techniques extract matrix material (e.g. Zr, Si, P, Ca, REE) that may form polyatomic species that are isobaric with the isotopes of interest, such as Pb (Ireland, 1995; Stern and Berman, 2001). While methods have been developed to correct for interferences, the corrections can be large. For EPMA techniques, considerable time must be devoted in quantifying the background for each sampling domain prior to analysis (e.g. Williams et al., 2007; Jercinovic et al., 2008; Spear et al., 2009). Furthermore, EPMA methods must assume concordance a priori because electron probes measure elemental concentrations, not isotopes. Third, LA-ICPMS and SIMS methods produce both elemental and isotopic fractionation as a result of differential vaporization and mobilization of extracted material (Hirata and Nesbitt, 1995; Horn et al., 2000; Kosler et al., 2001; Fletcher et al., 2010). Collectively, these "matrix effects" can affect the accuracy of measured dates by suppressing the ionization of targeted isotopes or producing isobaric interferences on measured masses.

Although they require significantly more analytical time to measure (hours vs. minutes), TIMS dates have long been interpreted as the "true" age of reference materials and are therefore commonly used as the benchmark age for calibrating other methods (e.g. Harrison et al., 1995). For TIMS analysis, samples are spiked with an isotopic tracer (the "isotope dilution" (ID) method) during dissolution. Spiked samples do not need to be calibrated to a separate reference material, thereby eliminating a major source of error. TIMS methods also do not confront the analytical challenge of "matrix effects" because this material is removed by column chemistry prior to analysis.

Despite its many advantages, TIMS analysis presents a few challenges. TIMS analyses do not commonly yield high spatial resolution and typical preparation methods remove the grains from their petrographic context. However, methods have been developed to measure multiple ID-TIMS ages from a single grain. Examples of these methods include fragmenting grains to analyze selected portions such as the tips of grains (e.g. Schärer and Allègre, 1982). More recently, X-ray maps are used to guide micro-sampling techniques via micro-milling (e.g. Corrie and Kohn, 2007).

Many iterations of method development for TIMS analysis have been published, typically aimed at selectively reducing or removing discordance. For example, the air abrasion method (Krogh, 1982) mechanically removes the outer layers of grains, often largely reducing the degree of discordance. However, air abrasion cannot remove discordant interior portions of grains, resulting in small amounts of residual discordance. Chemical abrasion TIMS ("CA-TIMS", e.g. Mattinson, 2003, 2005) is the latest technique for preferentially removing discordant portions of grains, both inside and out. The CA-TIMS method was pioneered with the accessory mineral zircon ($ZrSiO_4$) and uses high-temperature pre-dissolution annealing followed by one or more partial dissolution steps. The high-temperature annealing process converts metamict zircon to baddeleyite (ZrO_2), which is more easily dissolved than zircon. This process typically leaves a residue of closed-system zircon that, in the absence of inheritance, yields concordant results (e.g. Mundil et al., 2004).

Because of the success of CA-TIMS with zircon, we conducted a series of experiments to assess the application of CA-TIMS to U–Pb dating of monazite. In contrast to zircon, monazite is rarely metamict and is thought to self-anneal at low temperatures (Meldrum et al., 1998). However, previous work has demonstrated that thermal annealing produces structural recovery (Seydoux-Guillaume et al., 2002a), indicating that monazite does accumulate some radiation damage. Annealing at temperatures of 900–1100 °C yielded the most structural recovery as determined by Raman spectroscopy (Nasdala et al., 2002; Seydoux-Guillaume et al., 2002a). Although these temperatures are high, Pb diffusion studies have shown that a 100 μm radius monazite that cooled at 10 °C/Myr has a closure temperature of 1050 °C, which is 50 °C higher than zircon for equivalent conditions (Cherniak et al., 2004). These data suggest that a 48-hour annealing step at 1000 °C may repair the crystal lattice in monazite, thereby affording slower dissolution rates, without affecting the isotopic age. If thermal annealing converts radiation-damaged domains in monazite to a different phase – as seen with zircon – these domains should be chemically distinct and therefore identifiable via geochemical analysis.

The purposes of this study were to 1) evaluate the effects of annealing on the dissolution rate and isotopic age, and 2) determine whether the detailed, multi-step CA-TIMS approach reveals complexities in either age or composition that might be masked by single-step analysis. These questions were addressed through a side-by-side comparison of isotopic dates via multi-step TIMS (not annealed) and CA-TIMS (annealed), and measurement of rare earth element ratios for each dissolution step.

1.1. Sample selection criteria

Monazite samples were selected for this study because 1) their differences in composition (Fig. 1) reflect the range in natural monazite. For example, among the samples analyzed, ThO_2 ranges from ~3.5 to 15 wt.%; Ce_2O_3 from ~17 to 30 wt.%; Y_2O_3 from 0.5 to 2.5 wt.%; and CaO from 0.14 to 1.4 wt.% (Table 1; further EPMA data are compiled in the Data Repository). 2) Previous LA-ICPMS and SIMS analysis (Peterman et al., 2006) yielded relatively homogeneous isotopic data, despite elemental heterogeneity within some grains (e.g. Fig. 2). 3) The samples exist in sufficient quantity that they could be used as reference materials. Although the best reference materials are both isotopically and compositionally homogeneous, isotopic homogeneity is the most critical characteristic of a reference material. Because *554*, *Jefferson County*, *Madagascar*, *Amelia* and *Elk Mountain* were previously distributed as potential age reference materials, these samples were analyzed to evaluate their suitability.

1.2. Sample descriptions

554 is an accessory mineral from the peraluminous granite Catnip sill, a member of the Wilderness intrusive suite in the Santa Catalina Mountains, Arizona. This monazite is commonly used as a reference material for ion microprobe analysis (e.g. Harrison et al., 1999) and is the only sample for which whole grains—not fragments—were used in this study. Grains measure ~200 μm in diameter. In

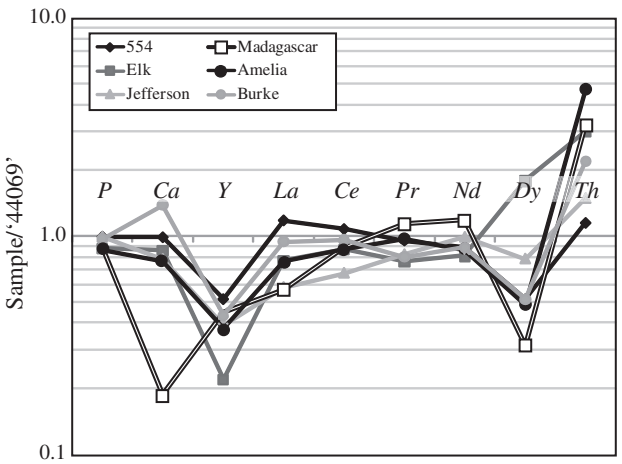

Fig. 1. Electron microprobe composition data of monazites analyzed in this study, normalized to monazite standard '44069' (Aleinikoff et al., 2006).

Table 1
Sample characteristics.

Sample name	Approx. age	Compositional characteristics (wt%) [a]				
	(Ma)	U_2O_3	ThO_2	Y_2O_3	CaO	Ce_2O_3
554	45 ± 1.3 [b]	0.02–0.11	3.8 ± 1.6	1.34 ± 0.17	0.84 ± .09	29.7 ± 0.7
	~44–47 [c]					
Amelia	274.6 ± 0.6 [d]	0.20 ± 0.02	15.1 ± 0.5	1.03 ± 0.06	0.64 ± 0.03	23.9 ± 0.2
			15.5 ± 0.3	0.98 ± 0.02	0.65 ± 0.02	24.1 ± 0.3
Burke	~365 [e]	0.51 ± 0.22	7.33 ± 1.26	1.13 ± 0.71	1.18 ± 0.14	26.5 ± 0.5
			8.1 ± 2.2	1.11 ± 0.61	1.29 ± 0.18	26.2 ± 0.8
Elk Mountain	~1391–1404 [f]	0.33 ± 0.04	10.2 ± 0.3	0.58 ± 0.02	0.73 ± 0.03	23.9 ± 0.2
			10.4 ± 0.2	0.61 ± 0.03	0.83 ± 0.02	23.8 ± 0.3
Jefferson County	365.5 ± 2.6 [d]	0.46 ± 0.35	5.00 ± 0.85	1.02 ± 0.32	0.66 ± 0.32	18.7 ± 0.9
	411 ± 12 [d]					
Madagascar	511.3 ± 4.9 [d]	0.41 ± 0.04	10.7 ± 0.3	1.26 ± 0.09	0.16 ± 0.02	23.9 ± 0.2
			9.7 ± 0.7	1.16 ± 0.07	0.16 ± 0.01	24.6 ± 0.3

[a] Electron microprobe data (data available in Data Repository 1).
[b] Harrison et al., 1995.
[c] Shakel et al., 1977.
[d] Peterman et al., 2006.
[e] Peterman, unpublished LA-ICP-MS data.
[f] J. Baldwin, unpublished TIMS data.

comparison with other monazites, *554* is low in U_2O_3 and ThO_2 (Table 1; full EMPA dataset in the Data Repository). Previous U–Th–Pb work on this sample yielded ages of 44–47 Ma (Shakel et al., 1977); the Th–Pb age of *554* is 45 ± 1.3 Ma (measured by M. Tatsumoto, as cited in Harrison et al., 1999). The age heterogeneity presents an opportunity to assess whether the CA-TIMS technique can elucidate complex monazite samples.

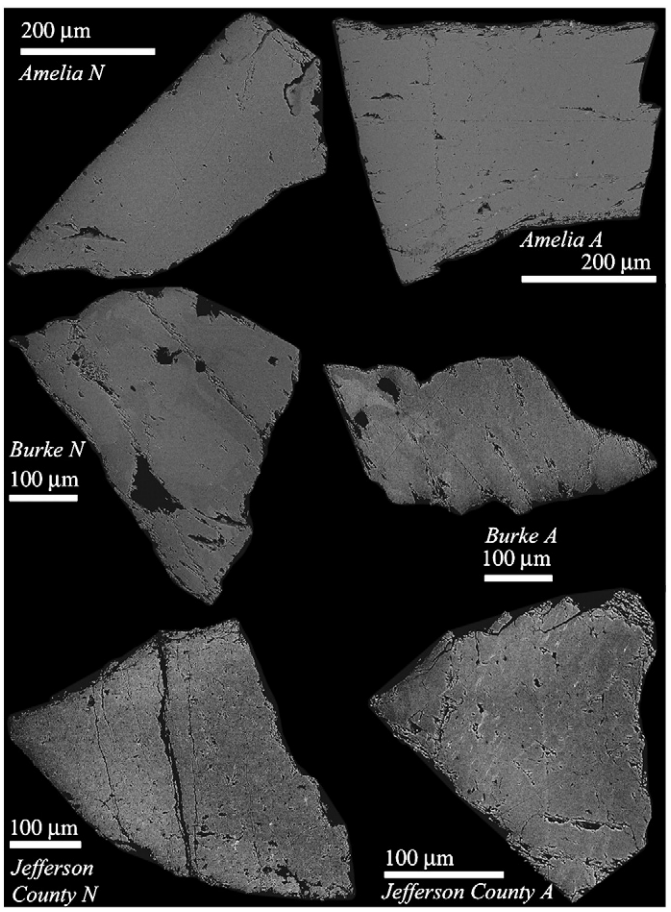

Fig. 2. Back-scattered electron (BSE) images of not-annealed (N) and annealed (A) monazite samples. *Amelia* does not have distinct compositional domains; *Burke* has compositional domains; and *Jefferson County* shows complex µm-scale chemical heterogeneity. Grain margins for annealed samples have more platy textures than not-annealed samples.

Amelia is a compositionally homogeneous Th-rich megacryst (Figs. 1 and 2; Table 1). Pegmatites from this mining region yielded a mica Rb–Sr age of 279 ± 14 Ma (Deuser and Herzog, 1962). Conventional TIMS analysis yielded a $^{206}Pb/^{238}U$ age of 274.58 ± 0.58 Ma (Table 1 and Data Repository). This sample was provided by the Smithsonian Institution and has previously been referred to as *Smithsonian* (Peterman et al., 2006).

Burke is a commercially purchased orange–yellow megacryst with patchy zoning and some (micro)cracks (Fig. 2); it is largely free of visible inclusions. It is the most Ca-rich monazite analyzed in this study (Fig. 1; Table 1), has more than one domain visible in backscattered electron (BSE) images (Fig. 2), and has greater variation in elemental composition than other samples (e.g. Y_2O_3, ThO_2; Table 1; Data Repository).

Elk Mountain is a portion of a pale to dark brown megacryst that has been widely distributed as an electron microprobe standard by M. Bersch (Univ. of Alabama). EPMA analyses of composition are homogeneous among and within grains. Analyses of a different aliquot of this sample yielded $^{207}Pb/^{206}Pb$ ages from 1391 to 1404 Ma and $^{206}Pb/^{238}U$ ages from 1413 to 1593 Ma (unpublished data, J. Baldwin, MIT).

Jefferson County is a portion of a brown megacryst that was also distributed as an electron microprobe standard by M. Bersch. Relative to the other samples, *Jefferson County* is depleted in light REE (Fig. 1; Table 1). It has patchy zoning and abundant (micro) cracks (Fig. 2). Previous LA-ICPMS data yielded an age of 365.5 ± 2.6 Ma (Peterman et al., 2006); conventional TIMS analysis yielded an equivalent $^{206}Pb/^{238}U$ age of 363.98 ± 0.74 Ma (Data Repository).

Madagascar is a brown–orange megacryst. Relative to other monazites, *Madagascar* is enriched in Pr and Nd, and depleted in Ca and Dy (Fig. 1; Table 1). LA-ICPMS and SHRIMP data suggested a crystallization age of ~492 Ma (Peterman et al., 2006). Conventional TIMS analysis yielded a $^{206}Pb/^{238}U$ age of 511.3 ± 4.9 Ma (Data Repository).

2. Methods

2.1. EPMA

Quantitative compositional analyses of the six monazite samples were conducted on Cameca SX-50 and Cameca SX-100 electron microprobes at UCSB, both operated at 15 kV accelerating voltage and 200 nA beam current. Monazite compositions are compared in Fig. 1; selected EPMA data are summarized Table 1. The full EPMA dataset is in the Data Repository.

2.2. Dissolution conditions

Several different sample-dissolution techniques were investigated in this study. Previous methods for monazite dissolution typically used concentrated HCl (~12 M) at high temperatures (>180 °C) and were targeted at complete dissolution. We experimented with acid strength (12 M, 6 M and 3.1 M HCl), temperature (120 °C, 100 °C and 80 °C) and step durations (12 and 6 h) to determine optimal conditions to permit multi-step analysis. All dissolution experiments were conducted with PARR digestion vessels. Not-annealed grain fragments of the *Jefferson County* and *Amelia* samples were ~80% dissolved with 6 M HCl at 120 °C for 12 h. Following identical dissolution conditions, grain fragments annealed for 48 h at 1000 °C were only 10–30% dissolved. The reduction in dissolution rate is consistent with results from zircon experiments (e.g. Mattinson, 2005). Because 10–30% dissolution in the first step represents a large proportion of the material, we used 3.1 M HCl and low initial temperature steps (80 °C) to yield sufficient dissolution steps to evaluate the CA-TIMS technique. The temperature and time for each dissolution step are listed in Table 2.

2.3. Sample dissolution and column chemistry

Multiple-grain aliquots of similarly sized grains or grain fragments of monazite samples *554*, *Amelia*, *Burke*, *Elk Mountain*, *Jefferson County* and *Madagascar* were selected for analysis. Approximately 10 grains (or grain fragments) of each sample were pretreated with a high-temperature annealing step (1000 °C for 48 h in air in high-purity alumina crucibles) and analyzed via multi-step CA-TIMS. An additional 10 grain fragments of the *Burke*, *Amelia* and *Jefferson County* samples were analyzed via multi-step TIMS without high-temperature pretreatment. The not-annealed grain fragments were optically identical to their annealed counterparts. In total, nine multi-grain (or grain fragment) samples were analyzed. Annealed samples are labeled "A"; not-annealed samples are labeled "N."

To remove surface contaminants, each sample was transferred into a 3 mL Teflon screw-top vial and rinsed with 1.5 mL 1.5 M HCl followed by two ultra-clean H_2O rinses. For each dissolution step, 50 μL of a 3.1 M HCl $^{205}Pb/^{235}U$ spike (converted from the commonly used "zircon" spike (e.g. Mattinson, 2005)) and 450 μL of 3.1 M HCl were added to each sample. The vials were then stacked three deep inside Teflon cups with an additional 1.5 mL 3.1 M HCl to normalize the vapor pressure inside and outside the sample vials. Teflon cups were placed inside PARR digestion vessels and loaded into ovens for dissolution. The paired annealed and not-annealed samples – *Jefferson County*, *Amelia* and *Burke* – underwent parallel dissolution conditions (i.e. the same temperature and time). Because *554* is much younger (Table 1) and smaller (average grain size ~200 μm diameter vs. 0.5–1 mm grain fragments for other samples), higher temperatures were used to yield enough U and Pb to measure reasonably precise ages on individual steps (Table 2). After every partial dissolution step, each sample was rinsed with ultra-clean water (at the lab bench) and then cleaned twice in 500 μL ultra-clean H_2O in the oven at the same temperature and time as the previous step. All rinse and cleaning solutions were pipetted off and discarded.

The Pb and U from each step were purified using the HCl ion exchange chemistry of Krogh (1973) with ~0.15 mL column resin beds. Column elutions were reserved for compositional analysis via ICP-MS (see Section 3.5). Pb and U were extracted from the columns together using ultra-clean H_2O and were collected in clean 5 mL Teflon beakers containing 6 μL 1 M H_3PO_4 (after Mattinson, 2005). After samples were fully dried in a HEPA-filtered drying box, Pb and U were loaded together onto outgassed Re filaments in 3.5 μL of silica gel.

2.4. U–Pb measurements

Samples were loaded in the UCSB Finnigan-MAT 261 TIMS and evacuated overnight. Each filament was preheated for 2 min at 2.0 A. U and Pb isotopic ratios were measured in static multi-collection mode. For most samples, ^{206}Pb, ^{207}Pb and ^{208}Pb were collected on Faraday cups while ^{204}Pb was simultaneously collected on a Spectromat ion-counting system; because the *Amelia* monazite has a high $^{204}Pb/^{206}Pb$ ratio, ^{204}Pb was collected on a Faraday cup.

The NIST 983 Pb standard was used to calibrate the ion-counter relative to the Faraday cups. Data were fractionation corrected using an assumed value of 0.12%/amu. The sample age was used to estimate the common-Pb correction following Stacey and Kramers (1975); $^{206}Pb/^{204}Pb_{common}$ and $^{207}Pb/^{204}Pb_{common}$ ratios are included in Table 2. Conservative error estimates of ±0.5 and ±0.2 were used for $^{206}Pb/^{204}Pb$ and $^{207}Pb/^{204}Pb$, respectively. Further details regarding error propagation and data analysis are provided in the Appendix A.

2.5. REE, P and Th measurements

Based on EPMA data (Data Repository), compositional domains within monazite grains can be identified by changes in relative concentrations of U, Th, Dy and Nd. To assess if age domains correlate with compositional domains, the composition and amount of monazite digested in each partial dissolution step were measured by analyzing the column elutions via ICPMS. Because each step dissolved different amounts of monazite, blank-corrected ratios (not concentrations) were used to identify changes in composition among the steps.

P and REE were measured on the Element XR at UC Santa Cruz, which has a sensitivity of 10^6 cps/ppb. Samples were spiked with 10 ppb Ho as an internal standard. The samples were aspirated with additional P-10 carrier gas (15 mL/min) to enhance P sensitivity and reduce oxide formation. ^{139}La, ^{140}Ce, ^{141}Pr, ^{143}Nd, ^{145}Nd, ^{146}Nd, ^{147}Sm, ^{149}Sm, ^{155}Gd, ^{157}Gd ^{161}Dy and ^{163}Dy were measured in low-resolution mode using ^{165}Ho as an internal standard; ^{31}P was measured in medium-resolution mode. ^{232}Th and ^{140}Ce were measured on the Element X-Series Quadrupole ICPMS at UC Santa Cruz; ^{140}Ce was used to intercalibrate the REE, P and Th data (Data Repository Table 2). The external precision of the ratios measured on the X-Series ICPMS was <0.2% (1σ) with a detection limit of 2 ppt; the instrument sensitivity is ~50,000 cps/ppb. Blank-corrected compositional data can be found in the Data Repository. An external isotope ratio precision of <0.4% (1σ) was determined by calculating the standard deviation of seven analyses of a monazite solution interspersed throughout the analytical run.

For this dataset, U/P, Th/P, Nd/P and Dy/P were used to determine if partial dissolution steps were sampling multiple compositional domains. Changes in U and Th might indicate dissolution of different age domains; Nd and Dy are the most reliable indicators of variation in REE for these six samples.

2.6. Single-step dissolution and TIMS analysis of Elk Mountain

Discrepancies between measured U/Pb and Pb/Pb ages for *Elk Mountain* merited further analysis. Eight new grain fragments were selected for analysis (grain images in Data Repository 2) and annealed at 1000 °C for 48 h prior to single-step dissolution. Each fragment was rinsed with water to remove surface contamination, spiked and dissolved in a PARR digestion vessel in ~500 μL of 3.1 M HCl at 200 °C for 12 h, ensuring complete single-step dissolution. The grain fragments were run through column chemistry and analyzed following methods described in Sections 3.4 and 3.5.

3. Results

3.1. SEM imaging

BSE imaging of annealed monazite shows the development of platy textures along the grain margins (Fig. 2). Although not-

Table 2
Experimental conditions and U–Pb geochronology data for CA-TIMS and multi-step TIMS analyses.

Sample	Anneal	Step conditions		U	P	Measured ratio[a]	Common Pb[b]		Calculated ages (Ma)				Calculated ratio
	°C/t(h)	°C	Hours	(%)	(%)	$^{206}Pb/^{204}Pb$	$^{206}Pb/^{204}Pb$	$^{207}Pb/^{204}Pb$	$^{206}Pb^{c}/^{238}U$	Error (2σ)	$^{207}Pb^{c}/^{235}U$	Error (2σ)	$^{232}Th/^{238}U$
Amelia A	1000/48						18.28	15.61					
A		80	12	2.1	3.0	64			277.0	6.4	285.8	33.2	354.6
B		80	12	1.7	2.4	36			257.2	15.4	227.8	95.2	284.0
C		80	12	1.9	6.0	71			274.0	5.4	289.3	28.1	367.6
D		90	12	2.7	3.5	71			272.9	5.3	281.0	27.6	381.2
E		90	12	4.2	4.9	74			273.4	5.1	272.0	26.6	389.7
F		110	12	3.0	3.8	74			274.9	5.1	313.6	25.8	345.8
G		120	6	5.4	5.5	69			270.8	5.6	269.2	34.1	388.0
H		120	6	6.3	6.2	75			270.8	5.0	270.6	29.1	395.7
I		130	6	9.2	8.3	78			271.4	4.8	271.6	26.0	402.7
J		140	6	8.8	8.4	79			270.4	4.6	253.4	25.7	431.7
K		150	6	13.1	12.3	81			273.0	4.5	276.6	24.1	403.0
L		150	6	7.1	6.3	84			271.6	4.3	265.4	25.2	429.3
M		160	6	8.3	7.4	88			273.2	4.1	288.5	22.0	396.2
N		160	6	8.4	7.3	84			272.3	4.3	261.0	24.2	438.9
O		160	6	6.8	5.7	90			271.5	4.0	260.8	23.1	434.3
P		160	6	5.6	5.2	91			273.4	3.9	277.0	24.3	417.5
Q		160	6	3.7	2.2	94			273.6	3.9	268.8	24.8	422.3
R		160	6	1.7	1.6	93			272.8	4.1	295.4	32.3	381.6
Amelia N	N/A						18.28	15.61					
A		80	12	11.0	10.3	19			96.8	196.5	105.6	273.9	38.1
B		80	12	8.2	8.6	91			273.9	3.9	277.1	23.7	384.6
C		80	12	8.9	9.1	97			274.7	3.6	292.0	18.2	367.8
D		90	12	10.0	9.7	93			273.4	3.8	274.9	20.1	385.9
E		90	12	14.7	14.2	93			272.4	3.8	264.4	21.4	402.6
F		110	12	10.5	10.3	94			272.9	3.7	273.3	20.2	390.4
G		120	6	14.8	13.8	94			272.5	3.8	267.2	20.5	399.2
H		120	6	12.2	12.2	91			272.2	3.9	275.3	22.3	382.7
I		130	6	7.3	7.9	86			273.2	4.2	277.0	23.9	364.6
J		140	6	2.3	3.7	80			270.4	4.9	274.2	51.4	337.4
Madagascar A	1000/48						17.93	15.58					
A		80	12	2.3	4.9	166			493.4	3.5	473.6	17.3	28.8
B		80	12	1.6	4.4	861			517.2	1.0	510.8	3.0	29.8
C		90	12	2.8	5.7	1150			516.1	0.7	512.2	2.2	29.7
D		90	12	2.5	4.8	1129			520.1	0.7	513.9	2.3	29.7
E		90	12	4.5	6.0	975			518.0	0.8	511.8	2.5	29.6
F		110	12	3.5	5.3	1132			520.4	0.7	513.9	2.3	29.7
G		120	6	6.9	7.0	1743			517.0	0.7	510.2	1.5	29.7
H		120	6	8.4	7.5	3071			516.5	0.6	511.7	1.0	29.7
I		130	6	10.5	8.6	4213			516.8	0.6	512.0	0.8	29.7
J		140	6	10.7	9.7	6357			516.9	0.5	512.0	0.7	29.8
K		150	6	13.3	10.5	6377			517.7	0.6	512.5	0.7	29.7
L		150	6	8.4	6.7	9675			518.1	0.6	513.6	0.6	29.7
M		160	6	12.6	8.4	9789			518.5	0.5	513.5	0.6	29.8
N		160	6	10.0	7.2	6736			517.9	0.6	512.8	0.7	29.6
O		160	6	2.1	3.2	4181			517.7	0.7	513.6	1.1	29.3
Burke A	1000/48						18.13	15.6					
A		80	12	1.3	2.2	869			353.0	0.6	354.7	2.1	15.5
B		80	12	1.0	2.0	3719			368.3	0.4	366.4	0.7	15.9
C		80	12	1.2	2.3	4072			369.9	0.4	368.1	0.6	15.8
D		90	12	1.8	2.7	5964			372.9	0.4	371.3	0.5	15.8
E		90	12	2.6	3.5	6280			381.0	0.4	377.4	0.5	15.9
F		110	12	2.8	3.7	6527			381.4	0.4	378.4	0.5	16.1
G		120	6	3.6	4.1	6834			376.9	0.5	374.0	0.6	16.1
H		120	6	4.1	4.9	8004			385.7	0.4	381.9	0.5	16.0
I		130	6	6.3	7.1	9133			376.7	0.4	374.1	0.5	16.3
J		140	6	12.5	12.0	11,418			373.7	0.4	371.5	0.4	16.2
K		150	6	11.5	11.0	13,054			377.3	0.4	374.6	0.4	16.0
L		150	6	8.6	8.2	14,507			378.0	0.4	375.2	0.4	15.9
M		160	6	10.4	9.8	16,256			377.3	0.4	374.5	0.4	15.7
N		160	6	14.8	12.2	18,672			374.3	0.4	372.2	0.4	14.6
O		160	6	8.4	7.0	17,899			375.0	0.4	372.8	0.4	14.0
P		160	6	6.3	5.2	16,909			375.8	0.4	373.6	0.4	14.1
Q		160	6	2.6	1.5	15,343			375.1	0.4	373.0	0.4	14.3
R		160	6	0.4	0.5	3224			373.6	0.6	374.0	1.8	15.2
Burke N	N/A						18.13	15.6					
A		80	12	9.0	9.1	192			356.9	5.0	354.9	25.9	16.5
B		80	12	7.2	7.5	10,658			372.4	0.4	370.2	0.5	17.7

Table 2 (*continued*)

Sample	Anneal	Step conditions		U	P	Measured ratio[a]	Common Pb[b]		Calculated ages (Ma)				Calculated ratio
	°C/t(h)	°C	Hours	(%)	(%)	$^{206}Pb/^{204}Pb$	$^{206}Pb/^{204}Pb$	$^{207}Pb/^{204}Pb$	$^{206}Pb^{c}/^{238}U$	Error (2σ)	$^{207}Pb^{c}/^{235}U$	Error (2σ)	$^{232}Th/^{238}U$
Burke N	N/A						18.13	15.6					
C		80	12	9.3	9.6	14,502			371.2	0.4	369.1	0.4	17.7
D		90	12	11.4	11.0	16,259			371.1	0.4	369.1	0.5	17.6
E		90	12	13.7	13.1	16,725			371.4	0.4	369.4	0.4	17.4
F		110	12	11.6	11.6	14,204			370.8	0.4	369.0	0.4	17.9
G		120	6	11.0	10.5	15,671			370.7	0.4	368.8	0.4	17.5
H		120	6	9.2	9.2	16,107			371.5	0.4	369.6	0.4	17.7
I		130	6	9.1	9.3	15,694			371.6	0.4	369.6	0.4	18.2
J		140	6	7.1	7.1	15,565			372.1	0.4	370.4	0.4	17.7
K		150	6	1.3	1.9	10,038			373.8	0.4	371.9	0.6	16.8
Elk Mountain A	1000/48						16.33	15.4					
A		80	12	5.5	3.1	9986			2027.4	2.2	1732.5	2.0	19.4
B		80	12	3.7	2.8	9231			2239.7	2.4	1834.7	2.2	25.0
C		80	12	3.5	3.8	9829			2309.9	2.5	1870.5	2.2	29.5
D		90	12	4.0	4.7	10,388			2428.5	2.6	1925.5	2.3	35.5
E		90	12	5.5	7.3	11,012			2443.2	2.9	1933.2	2.5	39.9
F		110	12	5.9	8.0	11,866			2305.3	2.5	1873.7	2.2	42.6
G		120	6	6.0	7.7	11,879			2083.1	2.5	1772.0	2.6	43.2
H		120	6	8.1	9.6	12,482			1898.0	2.6	1679.8	2.4	42.8
I		130	6	10.2	10.5	13,443			1691.9	2.1	1568.5	2.1	40.9
J		140	6	15.9	14.0	15,397			1603.7	2.2	1517.7	2.2	40.6
K		150	6	18.5	16.9	15,424			1576.1	2.4	1499.5	2.4	40.8
L		150	6	7.8	6.8	16,393			1561.8	1.9	1491.1	1.9	41.3
M		160	6	5.1	4.6	16,471			1545.9	1.7	1481.3	1.8	41.2
N		*160*	*6*	*0.0*	–	*1504*			*1513.2*	*11.5*	*1466.3*	*12.6*	*40.9*
554 A	1000/48						18.6	15.6					
A		80	12	4.5	4.2	30			36.8	3.5	47.0	23.5	52.2
B		80	12	4.3	4.4	106			46.1	0.6	38.3	3.3	149.5
C		90	12	4.5	5.2	123			44.3	0.4	42.6	2.6	151.6
D		100	12	8.7	9.3	125			45.0	0.4	46.3	2.5	153.6
E		100	12	8.4	10.0	112			46.8	0.5	48.5	3.0	154.7
F		120	12	8.1	9.4	140			47.0	0.4	41.8	2.3	201.2
G		130	6	10.6	12.6	146			47.4	0.4	45.2	2.2	192.7
H		130	6	11.4	14.0	179			49.5	0.3	48.6	1.8	196.2
I		*140*	*6*	*16.6*	–	*504*			*121.3*	*0.3*	*125.6*	*1.4*	*69.1*
J		150	6	13.5	16.8	175			49.9	0.3	47.4	1.9	226.5
K		160	6	9.3	13.6	122			50.8	0.5	43.6	2.9	256.8
L		*160*	*6*	*0.2*	–	*51*			*51.2*	*1.8*	*66.1*	*15.7*	*119.8*
Jefferson County A	1000/48						18.1	15.6					
A		80	12	7.2	4.9	1259			243.2	0.4	254.5	1.1	7.4
B		80	12	4.1	5.8	2767			347.4	0.4	345.5	0.8	9.9
C		80	12	2.7	5.0	2800			361.2	0.4	358.9	0.8	11.4
D		90	12	5.9	6.8	3951			369.6	0.4	364.9	0.6	9.9
E		90	12	7.0	7.8	4475			382.1	0.4	375.2	0.6	9.6
F		110	12	8.3	8.5	5540			373.0	0.4	367.3	0.5	9.6
G		120	6	13.6	11.5	6601			370.9	0.4	365.8	0.5	9.3
H		120	6	17.8	15.1	7991			368.1	0.4	363.0	0.5	9.4
I		130	6	16.8	17.5	9216			366.0	0.4	361.4	0.5	10.5
J		140	6	12.2	12.6	10,153			365.2	0.4	360.6	0.4	10.4
K		150	6	4.3	4.6	8015			363.9	0.5	359.0	0.6	7.9
L		*150*	*6*	*0.0*	–	*410*			*439.6*	*3.9*	*405.9*	*10.4*	*6.9*
Jefferson County N	N/A						18.1	15.6					
A		80	12	33.4	16.0	609			903.7	7.2	760.3	10.2	4.4
B		80	12	9.4	13.2	8499			362.4	0.4	359.1	0.5	22.3
C		80	12	9.0	12.5	10,902			362.1	0.4	358.9	0.4	21.8
D		90	12	11.5	14.3	10,924			360.7	0.4	357.8	0.4	20.1
E		90	12	12.1	16.7	11,003			364.6	0.4	361.3	0.4	20.1
F		110	12	11.7	14.4	11,728			361.2	0.4	358.1	0.4	18.6
G		120	6	9.6	8.0	10,743			359.6	0.4	357.1	0.6	18.1
H		120	6	3.1	4.1	11,437			359.2	0.4	356.7	0.5	20.9
I		130	6	0.2	0.7	2911			358.2	0.7	360.5	4.0	23.2

The acid used in all steps was 3.1 M HCl.

[a] Fractionation and spike corrected ratio.

[b] Calculated following Stacey and Kramers (1975).

[c] Analyses in italics were either contaminated or contained too little U to calculate meaningful ages.

annealed grains also have platy textures along the margins, they are less developed than on the annealed grains. BSE images of the annealed *Jefferson County* grain fragment also contain white wisps that are not evident in the not-annealed sample; these wisps may indicate recrystallization, but the scale of these features is too small to directly analyze via SEM or EPMA.

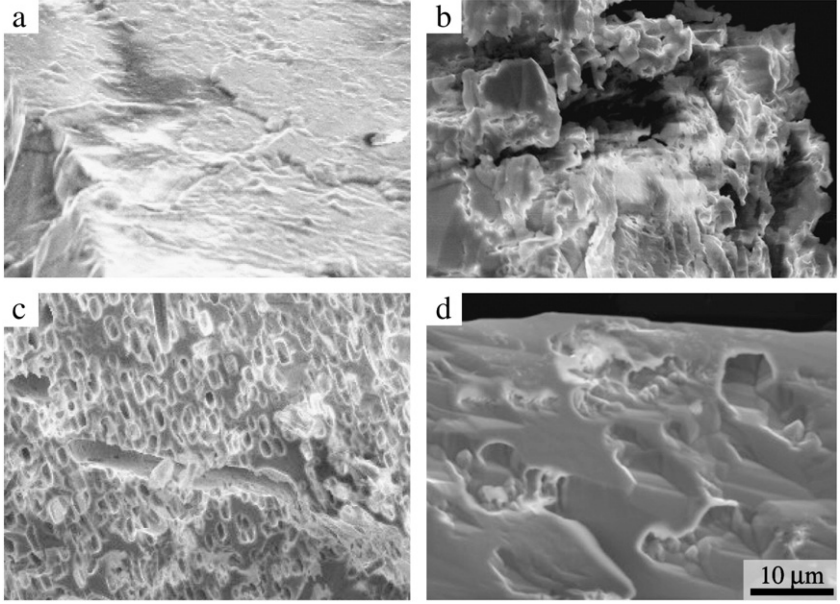

Fig. 3. Secondary electron images of *Jefferson County* and *Amelia* monazites show a range of etching textures resulting from partial dissolution. Annealing conditions were 48 h at 1000 °C in air. Partial dissolution conditions were 120 °C for 12 h in 6 M HCl for both samples. a) Annealed *Jefferson County* monazite prior to partial dissolution; broken grain margins and rough surfaces are common. b) Etched, annealed *Jefferson County* monazite. Partial dissolution was heterogeneous with cauliflower-like etch pits. c) Etch pits in the not-annealed *Amelia* monazite have an apparent preferred orientation and shape. d) Etch pits in annealed *Amelia* monazite are larger than in the not-annealed grain, but fewer, resulting in less dissolution. Etching is less extensive on the annealed *Amelia* grain than the annealed *Jefferson County* grain. All images are at the same scale.

Secondary electron (SE) images provide a qualitative indication of the effect of annealing on monazite and monazite dissolution patterns. Prior to dissolution, grains are commonly devoid of holes or pits, but locally have rough surfaces or fracture planes (*Jefferson County*; Fig. 3a). Partial digestion of the annealed *Jefferson County* monazite produced etch pits and significant removal of material from the interior and exterior of the grain fragment (Fig. 3b). Not-annealed (Fig. 3c) and annealed (Fig. 3d) fragments of the more crystalline *Amelia* monazite exhibit different responses to partial dissolution. In the not-annealed aliquot, etching followed microcracks and produced small (1–2 μm deep) etch pits throughout the grain fragment. In contrast, the larger etch pits (5–10 μm) in the annealed fragments are apparently restricted to the outermost portion of the fragment. The volume fraction of dissolved material is greater in the not-annealed aliquot than in the annealed aliquot. In both samples, acid primarily followed pre-existing lines of weakness (e.g. microcracks, crystal defects).

3.2. Geochronology and compositional data

The calculated dates for each dissolution step are reported in Table 1 and plotted in Figs. 4–9. CA-TIMS plots commonly follow the convention of Ar step-heating diagrams where the width of each box is proportional to the amount of sample dissolved in each step (e.g. Fig. 4, Mattinson, 2005); for monazite, the percent of total P is used as a proxy for the amount dissolved per step. The height of the box represents 2σ uncertainty.

For zircon CA-TIMS plateau diagrams, the plateau age is calculated as the weighted mean of sequential, concordant steps (e.g. Rioux et al., 2007). However, because monazite strongly partitions Th during (re)crystallization, the relatively short-lived ^{230}Th isotope – an intermediate decay product of ^{238}U decay – is also strongly partitioned into monazite, where it produces unsupported ^{206}Pb (e.g. Schärer, 1984; Parrish, 1990). Unsupported ^{206}Pb produces reversely discordant data, the magnitude of which is determined by the amount of ^{230}Th incorporated in monazite during (re)crystallization. Therefore, the "concordant" criteria used to calculate a weighted mean plateau age for zircon should not be applied to monazite. Instead, a weighted-mean plateau age is calculated according to the following five criteria summarized from Ludwig (2003): 1) a plateau is composed of three or more contiguous steps, 2) the probability-of-fit of the weighted-mean plateau age is greater than 5%, 3) the slope of the error-weighted line through the plateau is not different from zero at 5% confidence, 4) the dates of the two outermost plateau steps are not significantly different (at 1.8σ) than the weighted-mean plateau age (for plateaus with 6 or more steps), and 5) the outermost steps do not have non-zero slopes (at 1.8σ) with the same sign (for plateaus with 9 or more steps). Plateau ages that meet these criteria are compiled in Table 3.

In Figs. 4–9, steps included in the calculated plateau age are filled. Annealed samples are red (^{206}Pb/^{238}U) and purple (^{207}Pb/^{235}U); not-annealed samples are dark blue (^{206}Pb/^{238}U) and light blue (^{207}Pb/^{235}U). Compositional data from each dissolution step are plotted below the geochronology data (Figs. 4–9). As with the geochronology data, the width of the box is proportional to P measured in that step. Because each step dissolved different amounts of monazite, blank-corrected ratios (not concentrations) were used to depict changes in composition among the steps. Based upon BSE imaging and EPMA data, four elemental ratios were selected to provide representative information about variability among steps—Nd/P, Dy/P, Th/P and U/P. Nd and Dy were the most reliable indicators of variation in REE among the six samples; changes in U and Th might indicate dissolution of different age domains.

Conventional, Wetherill (1956), concordia diagrams for each sample are also plotted. These are preferable to Tera–Wasserburg diagrams for monazite because visual assessment of the effect of unsupported ^{206}Pb is not hindered by the common/^{206}Pb axes in Wetherill diagrams.

3.3. Amelia

Amelia A (annealed; Fig. 4a) yielded a ^{206}Pb/^{238}U plateau age of 274.29 ± 0.60 Ma (MSWD = 1.07; Table 3). Because the measured ^{206}Pb/^{204}Pb for this sample ranges from 36 to 94 (Table 2), the calculated dates are sensitive to common-Pb corrections. *Amelia N* (not annealed; Fig. 4b) gave an equivalent ^{206}Pb/^{238}U plateau age of 274.67 ± 0.71 Ma (MSWD = 0.80; Table 3). The ^{207}Pb/^{235}U plateau

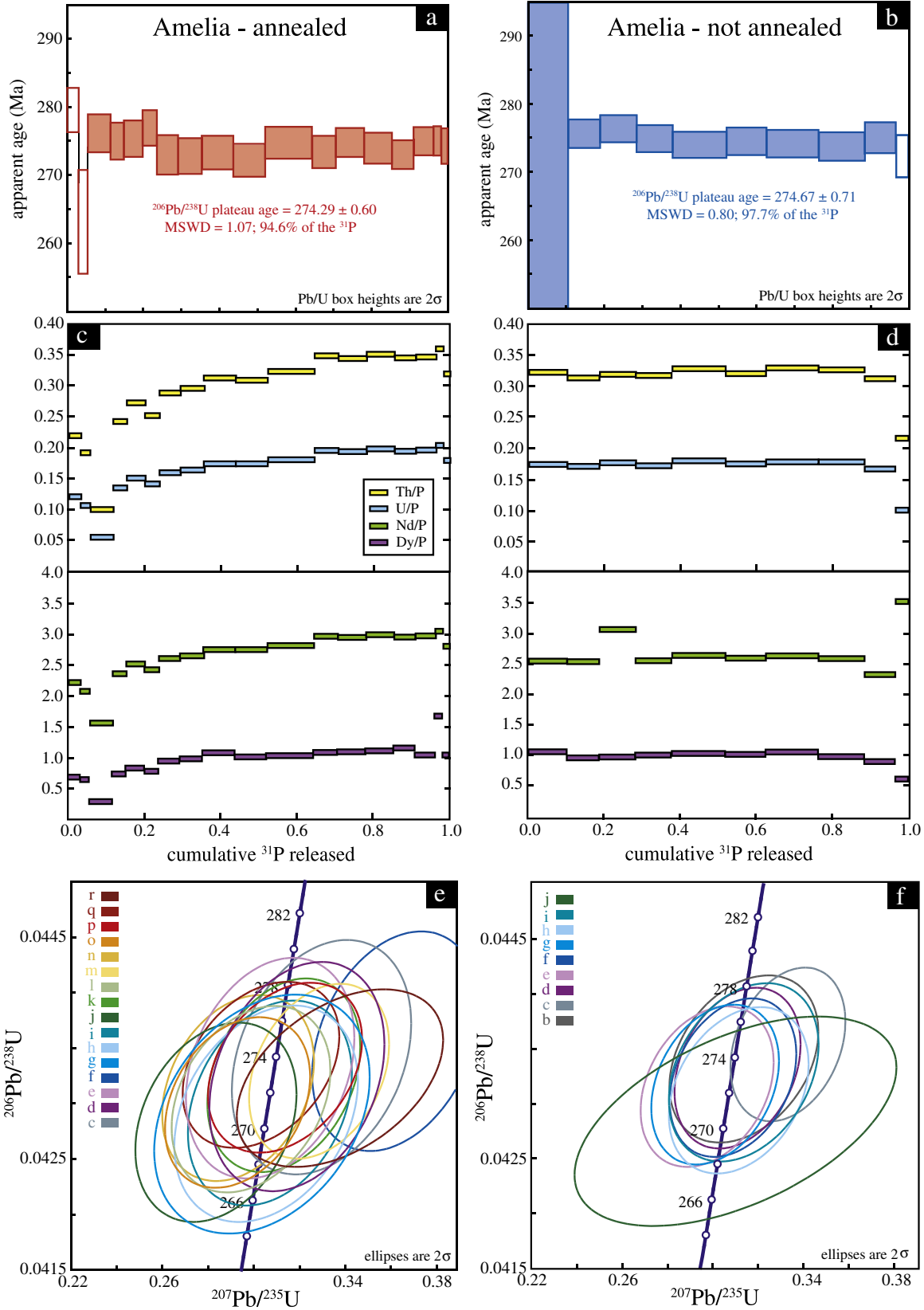

Fig. 4. *Amelia*. Apparent age spectra: (a) annealed, (b) not-annealed; compositional data: (c) annealed, (d) not-annealed; Wetherill concordia: (e) annealed, (f) not-annealed. Steps A-B are excluded from (e); step A is excluded from (f).

ages for *Amelia A* and *Amelia N* are equivalent at 275.6 ± 6.4 Ma (MSWD = 1.3) and 275.5 ± 7.3 Ma (MSWD = 0.87), respectively (Table 3). Errors on the individual $^{207}Pb/^{235}U$ measurements for this sample are large (~25 Ma), owing to high common-Pb and low U. To prevent visually obscuring the more precise analyses, the $^{207}Pb/^{235}U$ data are not plotted with the $^{206}Pb/^{238}U$ data, but all steps are

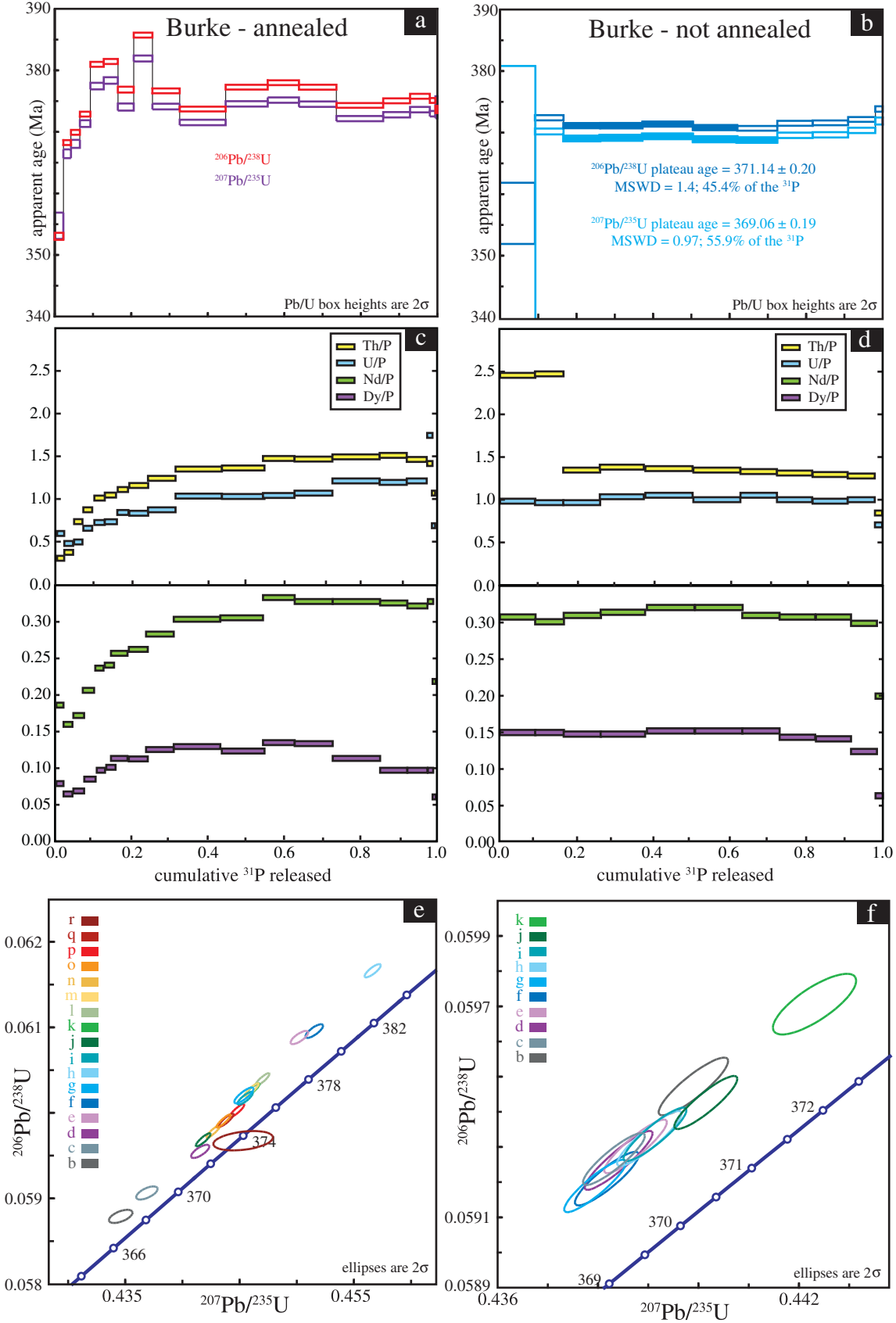

Fig. 5. *Burke*. Apparent age spectra: (a) annealed, (b) not-annealed; compositional data: (c) annealed, (d) not-annealed; Wetherill concordia: (e) annealed, (f) not-annealed. Step A is excluded from (e) and (f).

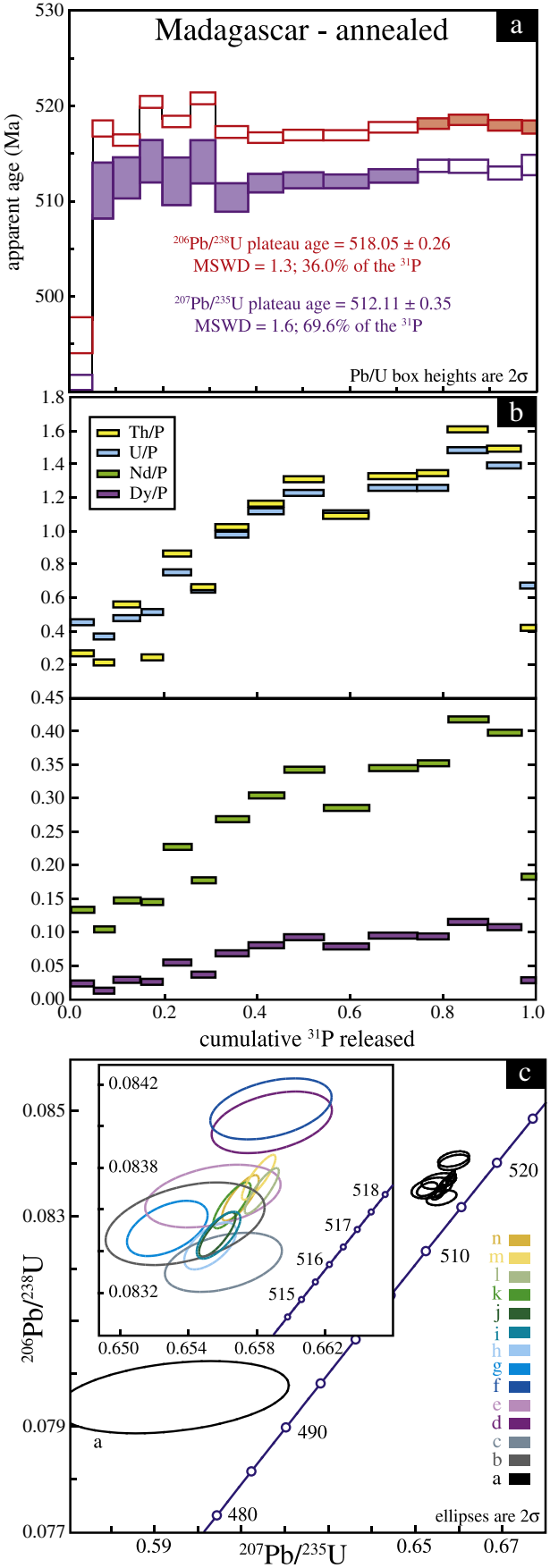

Fig. 6. *Madagascar*. Apparent age spectra (a); compositional data (b); Wetherill concordia (c).

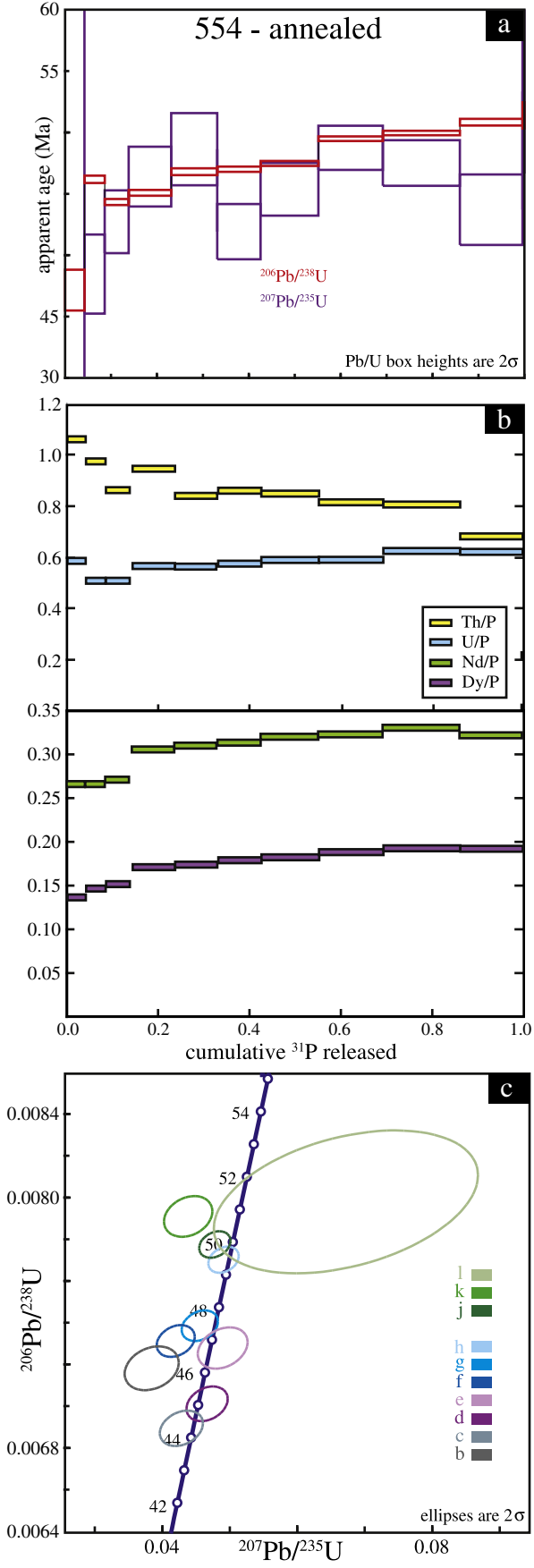

Fig. 7. *554*. Apparent age spectra (a); compositional data (b); Wetherill concordia (c). Steps A and I are excluded from (c).

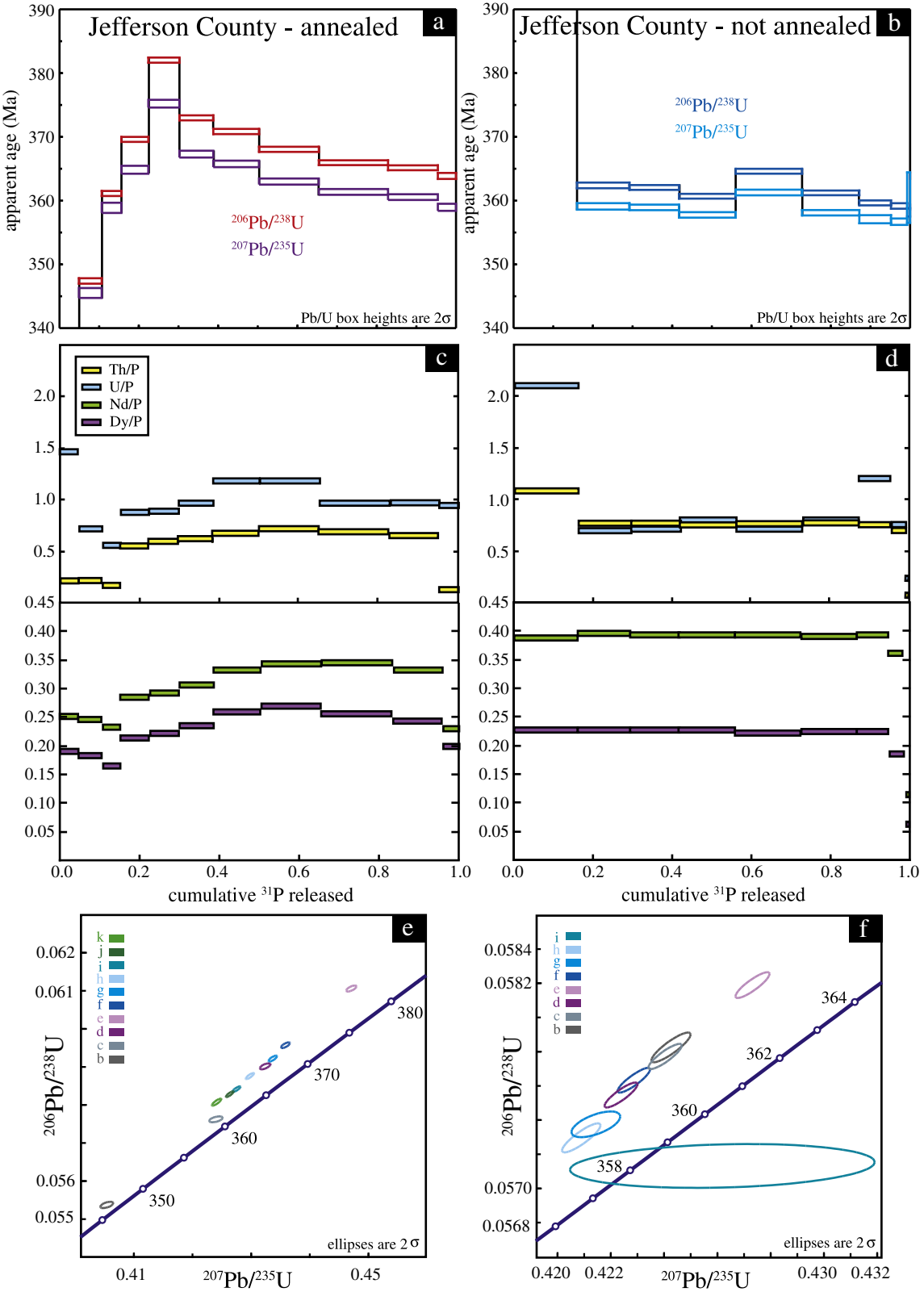

Fig. 8. *Jefferson County*. Apparent age spectra: (a) annealed, (b) not-annealed; compositional data: (c) annealed, (d) not-annealed; Wetherill concordia: (e) annealed, (f) not-annealed. Step A is excluded from (e) and (f).

included in Table 2. Step A of *Amelia N* (~10% of the total P) is younger than subsequent steps and has the most common Pb ($^{206}Pb/^{204}Pb = 19.1$). Because of the large error on this analysis (attributed to high common Pb), the date is within error of the other steps. Step B of *Amelia A* gave the youngest date with the largest error and highest common Pb ($^{206}Pb/^{204}Pb = 36.4$). The plateau ages for *Amelia*

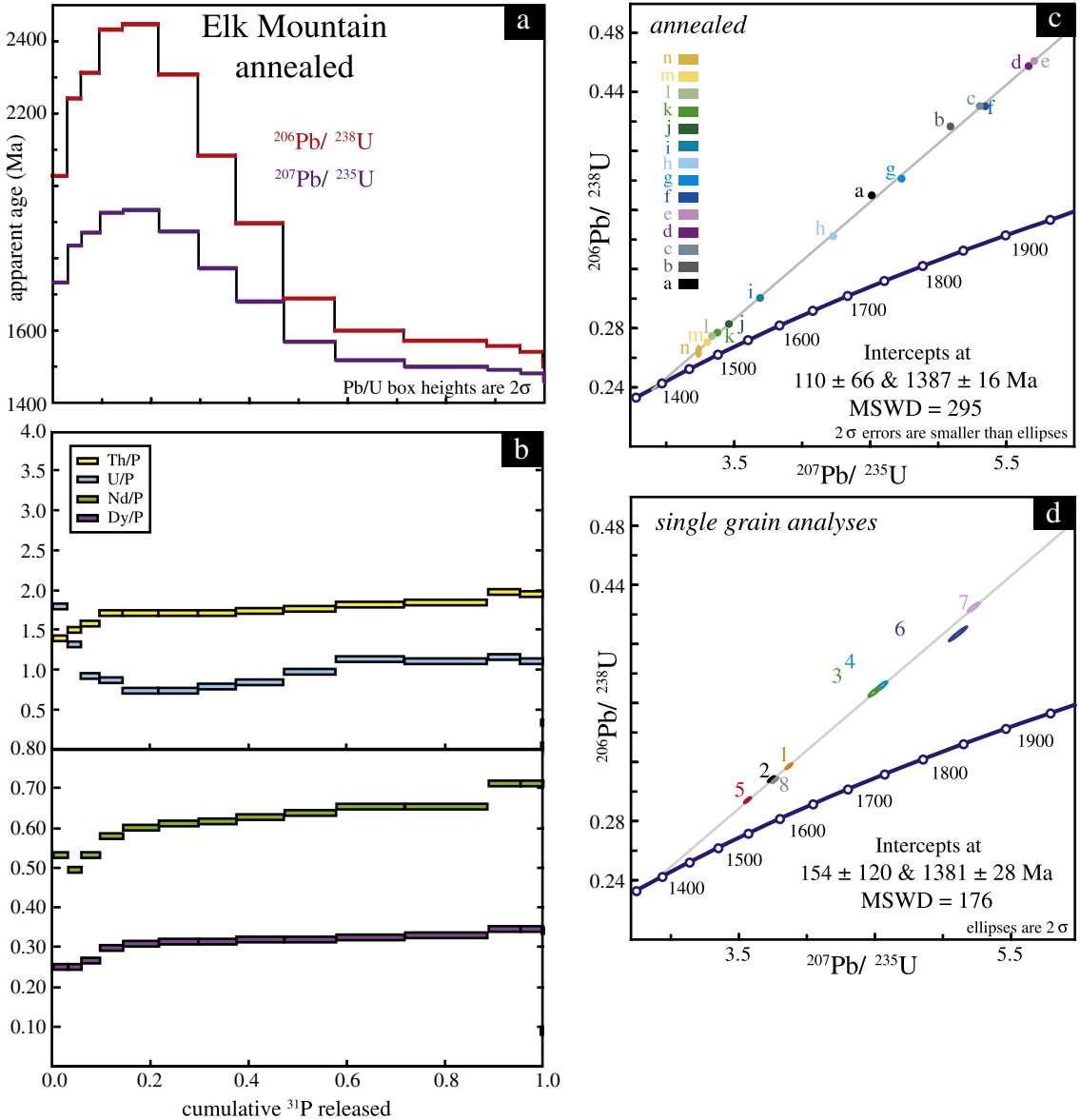

Fig. 9. *Elk Mountain*. Apparent age spectra (a); compositional data (b); Wetherill concordia for CA-TIMS analyses (c); single-step dissolution analyses (d). Because the error ellipses for the CA-TIMS data are too small to plot, they have been replaced with uniform sized spots (except for "n").

A and *Amelia N* are equivalent. Nearly all analyses of *Amelia A* and *Amelia N* (Fig. 4e–f) samples are "technically" concordant; i.e., in agreement within analytical errors, but given the large uncertainties in the ^{207}Pb/^{235}U dates, the apparent concordance has little meaning.

Amelia A and *Amelia N* have the same integrated elemental composition, but yield different compositional spectra. The first three steps of *Amelia A* decrease in Nd/P, Dy/P, Th/P and U/P, and all subsequent steps slowly increase (Fig. 4c). Although there is some variability in composition from step-to-step for *Amelia N* (Fig. 4d), the data are less variable than the *Amelia A* data.

3.4. Burke

Burke A (annealed) yielded crankshaft-style age spectra (Fig. 5a). The first four steps are younger than the mean age of the remaining steps. *Burke N* (not annealed) gave a ^{206}Pb/^{238}U plateau age of 371.14 ± 0.20 Ma (MSWD = 1.4; Fig. 5b; Table 3). The ^{207}Pb/^{235}U plateau age is slightly younger at 369.06 ± 0.19 Ma (MSWD = 0.97; Table 3). The consistent offset between ^{206}Pb/^{238}U and ^{207}Pb/^{235}U dates and the reverse discordance of nearly all steps for both *Burke A* and *Burke N* (Fig. 5e–f) are presumably related to unsupported ^{206}Pb. Whereas the *Burke N* ellipses tend to cluster, *Burke A* ellipses are dispersed along a line parallel to concordia.

Elemental analyses indicate divergent patterns for *Burke A* and *Burke N*. *Burke A* (Fig. 5c) is characterized by steadily increasing Nd/P and U/P ratios whereas *Burke N* has more consistent Nd/P and U/P ratios. Th/P follows the U/P trend for *Burke A*, but the first two steps of *Burke N* have a higher Th/P than subsequent steps. Dy/P yielded a curved pattern for *Burke A*; in contrast, Dy/P is constant for ~70% of *Burke N* until the last four steps, which decrease (Fig. 5d).

3.5. Madagascar

Madagascar (annealed only; Fig. 6a) gave a ^{206}Pb/^{238}U plateau age of 518.05 ± 0.26 Ma (MSWD = 1.3; Table 3) and a ^{207}Pb/^{235}U plateau age of 512.11 ± 0.35 Ma (MSWD = 1.6; Table 3). The offset between ^{206}Pb/^{238}U and ^{207}Pb/^{235}U dates is presumably related to unsupported ^{206}Pb; the magnitude of offset between ^{206}Pb/^{238}U and ^{207}Pb/^{235}U

Table 3
Plateau age data summary.

Sample	$^{206}Pb/^{238}U$				$^{207}Pb/^{235}U$			
	Plateau age (Ma)	Error (Ma)	MSWD	%P	Plateau age (Ma)	Error (Ma)	MSWD	%P
Amelia A	274.29	0.60	1.07	94.6	275.6	6.4	1.3	100
Amelia N	274.67	0.71	0.80	97.7	275.5	7.3	0.87	100
Burke A	–	–	–	–	–	–	–	–
Burke N	371.14	0.20	1.4	45.4	369.06	0.19	0.97	55.9
Madagascar A	518.05	0.26	1.3	36.0	512.11	0.35	1.6	69.6
554 A	–	–	–	–	–	–	–	–
Jefferson County A	–	–	–	–	–	–	–	–
Jefferson County B	–	–	–	–	–	–	–	–
Elk Mountain A	–	–	–	–	–	–	–	–

dates is equivalent to the offset observed via conventional TIMS (Data Repository). Of the $^{206}Pb/^{238}U$ step analyses, A is the youngest; the next six steps (B–G) define a crankshaft pattern. Steps H–M gradually increase, whereas the last two steps are slightly younger. Although the data cluster together on the concordia diagram, all are reversely discordant (Fig. 6c). Elemental analyses of the steps show variable, but increasing ratios (Fig. 6b), except for the last step, which is significantly lower.

3.6. 554

The $^{206}Pb/^{238}U$ data are more precise than the $^{207}Pb/^{235}U$ data for *554* (annealed only) because the sample is Miocene. Step A has large errors for both $^{206}Pb/^{238}U$ and $^{207}Pb/^{235}U$ (Fig. 7a). Steps C–K progressively increase from ~44.3 to 50.8 Ma. Step I is significantly older (121.3 Ma; $^{206}Pb/^{238}U$), but was excluded from Fig. 7a, b and c because it was likely contaminated (Table 1). Six of the individual analyses are concordant (Fig. 7c) and four are reversely discordant (Fig. 7c).

The Nd/P and Dy/P broadly mimic the Pb/U trends, with steadily increasing values (Fig. 7b). Apart from the slightly enriched first step, U/P also increases towards the last steps. Th/P follows the opposite trend.

3.7. Jefferson County

The patterns of the apparent age spectra for *Jefferson County A* (annealed) and *Jefferson County N* (not annealed) differ (Fig. 8a–b). Steps A–E of *Jefferson County A* increase to a maximum $^{206}Pb/^{238}U$ step age of 382.1 ± 0.4 Ma and then decrease to 363.9 ± 0.5 Ma (step K). In contrast, *Jefferson County N* has a significantly older first step followed by a narrow range of dates from 358.2 to 364.6 Ma; these steps do not yield a plateau age. The $^{206}Pb/^{238}U$ dates are older than the $^{207}Pb/^{235}U$ dates for both *Jefferson County A* and *Jefferson County N* (Fig. 8a–b), presumably because of unsupported ^{206}Pb.

The Nd/P, Dy/P, Th/P and U/P ratios of the first three dissolution steps of *Jefferson County A* decrease (Fig. 8c) whereas subsequent steps yield a hump-shaped pattern. In contrast, the U/P, Dy/P and Nd/P ratios of *Jefferson County N* are broadly consistent. Although Th/P is more variable than the other ratios, it is still more homogeneous in *Jefferson County N* than *Jefferson County A*.

All analyses are reversely discordant, except for the less precise *Jefferson County N* step I (Fig. 8e–f). The error ellipses of the not-annealed analyses overlap whereas the annealed analyses do not.

3.8. Elk Mountain

The grain fragments of *Elk Mountain* analyzed via CA-TIMS methods yielded apparent age spectra that rise and fall within a range of ~1515 Ma to 2445 Ma (Fig. 9a). The spectra start at ~2025 Ma ($^{206}Pb/^{238}U$) and ~1730 Ma ($^{207}Pb/^{235}U$) and increase by ~20% in steps A–E. From steps F–J, the $^{206}Pb/^{238}U$ and $^{207}Pb/^{235}U$ dates fall from ~2445 to ~1600 Ma and ~1935 to ~1515 Ma. The second halves of the spectra decrease progressively from ~1600 to ~1515 ($^{206}Pb/^{238}U$) and ~1515 to 1465 Ma ($^{207}Pb/^{235}U$). Collectively, the CA-TIMS steps form a discordia line with an upper intercept of $\sim 1387 \pm 16$ Ma and a lower intercept of 110 ± 66 Ma (Fig. 9c). Steps A–E progress away from concordia along the discordia line, whereas subsequent steps move back down the discordia line towards the upper intercept. All steps are moderately to strongly reversely discordant, far beyond what could be attributed to unsupported ^{206}Pb.

The Th/P, Nd/P and Dy/P spectra have steadily increasing ratios (Fig. 9b). The U/P ratios follow the reverse pattern of the apparent age spectra—where the U/P ratio decreases, the Pb/U ratio, and thus the apparent age, increases.

The eight grain fragments that were single-step digested are all strongly reversely discordant (Fig. 9d). Collectively, they define a discordia line that has intercept ages of 1381 ± 28 Ma and 154 ± 120 Ma.

4. Discussion

4.1. Effect of annealing on dissolution rates

To directly evaluate the effect of annealing on dissolution rate, both aliquots of annealed and not-annealed monazite need to be identical. Aliquots of the *Burke* and *Amelia* monazites are well matched, but the *Jefferson County* aliquots apparently differ in elemental composition (Fig. 8c and d; Data Repository). Nevertheless, the proportion of monazite dissolved in the first step for all three annealed samples is significantly greater for the not-annealed aliquots than the annealed aliquots: 9% vs. 2% for *Burke*; 10% vs. 3% for *Amelia*; and 16% vs. 5% for *Jefferson County* (Figs. 4a,b, 5a,b, 8a and b). These data suggest that annealing reduced the solubility of monazite, which is consistent with previous studies that have demonstrated that thermal annealing repairs structural damage caused by radiation (e.g. Seydoux-Guillaume et al., 2002a). Although the specific mechanism by which this occurred was not determined, the differences in etch pit morphologies between annealed and not annealed grains (Fig. 3) suggest that annealing repairs microcracks, dislocations, or lattice damage from alpha-recoil and fission.

4.2. Annealing, composition and age

The three samples that were analyzed via both CA-TIMS and multi-step TIMS permit assessment of the effects of annealing on composition and apparent age. Not-annealed samples tend to have broadly homogeneous chemical spectra (e.g. Figs. 4d, 5d and 8d). In contrast, the annealed counterparts tend to yield much more complex spectra (Figs. 4c, 5c and 8c). Because the not-annealed and annealed aliquots of the *Burke* and *Amelia* monazites are elementally well matched (Data Repository), the difference in morphology of the elemental spectra between Fig. 4c vs. 4d and Fig. 5c vs. 5d is most likely attributed to annealing. The *Jefferson County* aliquots also yielded similar patterns to *Burke* and *Amelia*, but differences in chemistry between *Jefferson County A* and *Jefferson County N* may also affect dissolution.

Although not all six samples have not-annealed counterparts, the compositional spectra of all six samples either increase monotonically or are hump shaped. These patterns suggest that annealing affects how monazite dissolves; this is further supported by the variation in dissolution rates.

The effect of annealing on apparent age is less clear—for the *Amelia* monazite, the $^{206}Pb/^{238}U$ ages are equivalent, regardless of whether the sample was dated via CA-TIMS, multi-step TIMS or conventional TIMS analysis. The *Burke* monazite, however, yielded different apparent ages for the CA-TIMS and multi-step TIMS analyses. In *Burke A*, annealing appears to have induced a crankshaft pattern in apparent age (and

composition) that is not evident in *Burke N*. Although there are chemical differences between the *Jefferson County* aliquots, the annealed aliquot yielded more complex spectra than the not-annealed aliquot. *Jefferson County A* yielded a hump-shaped pattern in age and composition whereas *Jefferson County N* was more homogeneous, apart from the older first step (~960 Ma), which is also enriched in U and Th.

The relationship between variability in apparent age and composition is complex. BSE imaging and EPMA point analyses indicate that the *Burke* and *Jefferson County* samples have different compositional domains characterized by changes in Dy, Nd, Th and U content. Because monazite is often poly-metamorphic, compositional domains may differ in age (e.g. Williams et al., 2007). If partial dissolution steps were micro-sampling multiple age (and composition) domains, one might expect to see a correlation between apparent age and composition. Evidence of this is seen in the first step of the *Jefferson County N* sample, which yields an age of ~960 Ma (Fig. 8b) and is compositionally distinct in U/P and Th/P; Nd/P and Dy/P are chemically indistinguishable from younger steps (Fig. 8d). For all other samples, composition and apparent age of partial dissolution steps are not correlated. For example, the first step of *Burke* is significantly younger than all subsequent steps (Fig. 5a), but the compositional data show an increasing trend across the spectra, not an anomalous first step followed by more homogeneous steps. The same trend is evident in *Madagascar*—the first step is anomalously young (Fig. 6a), but there is no corresponding pattern in composition (Fig. 6b).

In general, variation in age cannot be linked to increases or decreases in a specific compositional parameter. Instead, only broad associations between patterns can be made. For example, annealed samples that generally do not yield plateau ages have curved or hump-shaped compositional patterns. Not-annealed samples have flat compositional spectra and, typically, a plateau age.

These data prompt the question of why the spectra of not-annealed monazite are simpler than those of annealed monazite. One possibility could be that (epitaxial) recrystallization, or dissolution/reprecipitation occurred during annealing and the newly formed crystals behaved differently. If epitaxial recrystallization occurred, the newly formed crystals might be visible along the grain exteriors in BSE (e.g. Seydoux-Guillaume et al., 2002a, 2002b); the BSE images are equivocal, however, showing platy new growth at the margins of the annealed grains (Fig. 2) as well as evidence of platy minerals on some of the not-annealed grains.

Annealing-induced recrystallization at the sub-micron scale should be reflected by changes in dissolution patterns because repaired crystal structures should respond differently to acid etching. As described in Section 4.1, annealed grains dissolve more slowly than not-annealed grains. However, not all samples contain the same initial radiation damage. The degree of initial radiation damage, therefore, might be a predictor of the extent of recrystallization. More-crystalline samples likely contain less accumulated radiation damage; thus the effects of annealing should be minimized, resulting in less recrystallization and reducing the possibility of chemical redistribution within a grain. More-crystalline samples would therefore yield more consistent apparent age spectra because the degree of recrystallization is lower (i.e. there is a smaller relative change in crystallinity from start to finish for the more-crystalline samples). The higher degree of disorder in the crystal lattice in the less-crystalline/more radiation-damaged samples may enhance recrystallization, resulting in more heterogeneous apparent age and compositional spectra. The divergence in behavior between the annealed and not-annealed monazites in this study may be explained by this hypothesis. *Amelia* is generally more crystalline than the other samples, is homogeneous in composition, and yielded homogeneous dates, regardless of how it was treated. The difference in compositional spectra for *Amelia A* and *Amelia N* would then reflect partial recrystallization induced by annealing (Fig. 4c).

In contrast to *Amelia*, *Jefferson County* is less crystalline, has patchy compositional domains and did not yield homogeneous dates. The white wisps in the annealed *Jefferson County* (Fig. 2) may be evidence of annealing-induced recrystallization. Furthermore, the heterogeneous compositional spectra may reflect annealing-induced larger-scale recrystallization of *Jefferson County A* (Fig. 8c).

Burke provides a middle ground between these end-member behaviors. It is more crystalline than *Jefferson County*, but has patchy compositional zoning. Annealed aliquots yielded heterogeneous age and composition spectra whereas not-annealed aliquots yielded plateau ages and more consistent composition spectra. Annealing apparently degrades *Burke*, but multi-step dissolution of not-annealed grain fragments yielded plateau ages, despite the presence of patchy compositional domains.

4.3. Elk Mountain

CA-TIMS analysis of the *Elk Mountain* monazite yielded unexpectedly complex age spectra that rise and fall between ~1500 Ma and 2400 Ma. All steps are moderately to strongly reversely discordant (Fig. 9c), far beyond what could be attributed to unsupported ^{206}Pb. The single-step dissolution data are also strongly reversely discordant and define a discordia line identical to the CA-TIMS data. Furthermore, not-annealed grains yielded an equivalent discordia line (unpublished data, J. Baldwin, MIT). The consistency of the Pb–Pb apparent ages among these datasets and the equivalence of the discordia lines suggest that 1) high-temperature annealing is not responsible for the discrepancy between U/Pb and Pb/Pb ages or the extreme reverse discordance, 2) the Pb–Pb system was likely undisturbed, and 3) the U–Pb system has been apparently compromised; a potential cause could be preferential removal of U at ~100 Ma.

4.4. Recommendations for use as monazite reference materials

Amelia is a good candidate for use as a Th-rich, U-poor monazite reference material. The ages are consistent with the Rb–Sr mica age (279 ± 14 Ma; Deuser and Herzog, 1962) and conventional TIMS data (274.6 ± 0.6 Ma; Table 1). Although the high Th content may preclude its use with some microbeam techniques (e.g. SIMS), advances in detector design (e.g. beam attenuation) may permit it to be used with certain instrumentation.

Burke has potential for use as a reference material. The not-annealed sample yielded a plateau age with homogeneous compositional release. Annealing appears to induce scatter in measured composition and age.

Because of the complex age patterns, *Jefferson County* should not be used as a reference material.

The isotopic complexity of the *Elk Mountain* monazite renders it unsuitable for use as a reference material. Instead, the similarity in discordia lines among CA-TIMS, annealed single step TIMS and conventional TIMS analyses (unpublished data, J. Baldwin, MIT) suggests that the age variation is most likely attributed to a geologic disturbance at ~100 Ma (the lower intercept) that preferentially removed U and left the Pb–Pb system intact.

Madagascar is a good candidate for use as a reference material, but the age discrepancy of ~6 Myr between CA-TIMS and conventional TIMS data suggests that there may be differences in age among grain fragments. Furthermore, the difference in $^{206}Pb/^{204}Pb$ ratios between the aliquots analyzed via CA-TIMS and conventional TIMS suggests heterogeneity among fragments of the megacryst. Further consideration for use as a reference material requires analysis of additional aliquots.

Because *554* is young (~45 Ma) and U poor (~400 ppm U), obtaining high-precision U–Pb ages can be analytically challenging. The weighted-mean ages (for non-contaminated steps) are 47.7 ± 1.5 Ma (MSWD = 94; $^{206}Pb/^{238}U$) and 45.5 ± 2.2 Ma (MSWD = 6.4; $^{207}Pb/$

^{235}U). Although these results are consistent with previous data (44–47 Ma; Shakel et al., 1977), the lack of an age plateau and the high MSWD values indicate that the dates do not form a single population and instead suggest (re)crystallization from ~45–50 Ma. Because it is heterogeneous and has ages known to a precision of only 5%, *554* should not be used as a reference material.

5. Conclusions

Multi-step partial dissolution of monazite can be an effective way to unravel the complex histories of poly-metamorphic grains. Annealing apparently reduces the solubility of grains by repairing structural damage of the crystal lattice; larger defects such as cracks or microcracks remain. The data suggest that annealing induces recrystallization that affects the style of dissolution and produces more variable age and composition spectra than observed with not-annealed samples. High-temperature annealing is therefore not recommended for monazite.

Step-wise digestion of monazite can reveal isotopic complexities that might be missed by single-step TIMS analysis or microbeam analyses, including discordance between $^{206}Pb/^{238}U$ and $^{207}Pb/^{235}U$ ages. The $^{207}Pb/^{235}U$ plateau ages afforded by multi-step CA-TIMS permit accurate age determinations that are unaffected by unsupported ^{206}Pb. The *Burke* and *Amelia* monazites may be suitable for use as reference materials.

Acknowledgments

Thanks to H. Berg, G. Seward, J. Hourigan and R. Franks for analytical assistance; M. Bersch (Univ. of Alabama) provided *Elk Mountain* and *Jefferson County*; M. Grove (Stanford University) provided *554*; J. Aleinikoff (USGS) provided *44069*; The Smithsonian Institution provided *Amelia*; and B. Schulz (ETH-Zurich) provided *Madagascar*. Thanks to Ian Fletcher and an anonymous reviewer for careful reviews, and to Laurie Reisberg for editorial handling. This research was funded by an NSF GRF awarded to Peterman, NSF EAR-0948158 to Peterman, NSF EAR-0549674 to Mattinson, and NSF EAR-0510453 to Hacker and Mattinson.

Appendix A. Methods for U–Pb error analysis

All errors for U–Pb analyses were calculated following Mattinson (1987). Uncertainties on each partial dissolution step (or bulk dissolution, for conventional TIMS data) are reported at 2σ and were calculated as:

$$2\sigma_{207/206} = \left\{ \left[2 * \mathrm{SE(M)}_{207/206}\right]^2 + [0.04\%]^2 + [2\sigma_{\mathrm{common}}]^2 \right\}^{1/2}$$

$$2\sigma_{206/238} = \left\{ \left[2 * \mathrm{SE(M)}_{205/206}\right]^2 + \left[2 * \mathrm{SE(M)}_{238/235}\right]^2 + [2\sigma_{\mathrm{common}}]^2 + [0.2\%]^2 \right\}^{1/2}$$

$$2\sigma_{207/235} = \left[\left(2\sigma_{206/238}\right)^2 + \left(2\sigma_{207/236}\right)^2 \right]^{1/2}$$

where SE(M) is the standard error of the mean of the measured ratio, 0.04% is the uncertainty in the $^{207}Pb/^{206}Pb$ fractionation correction, $2\sigma_{common}$ is the error associated with the common-Pb correction (described below) and 0.2% is the observed $^{206}Pb/^{238}U$ error as determined by in-house replicate analyses of well-characterized natural samples. Propagated common-Pb errors ($2\sigma_{common}$) include the precision of the $^{206}Pb/^{204}Pb$ measurement and conservative absolute errors of ±0.2 and ±0.5 for the assumed $^{207}Pb/^{204}Pb$ common and $^{206}Pb/^{204}Pb$ common. We assumed a common-Pb value based on the age of the sample, following Stacey and Kramers (1975). The 0.1% error in the $^{206}Pb/^{238}U$ analyses incorporates uncertainty in U and Pb fractionation corrections. Final sample ages and propagated errors were calculated as the weighted mean of the plateau steps, as defined in Isoplot 3.0/3.2 (Ludwig, 2003).

Appendix B. Supplementary data

Supplementary data to this article can be found online at http://dx.doi.org/10.1016/j.chemgeo.2012.04.006.

References

Aleinikoff, J.N., Schench, W.S., Plank, M.O., Srogi, L., Fanning, M.C., Kamo, S.L., Bosbyshell, H., 2006. Deciphering igneous and metamorphic events in high-grade rocks of the Wilmington Complex, Delaware: morphology, cathodoluminescence and backscattered electron zoning, and SHRIMP U–Pb geochronology of zircon and monazite. Geological Society of America Bulletin 118 (1/2), 39–64.

Catlos, E.J., Gilley, L.D., Harrison, T.M., 2002. Interpretation of monazite ages obtained via in situ analysis. Chemical Geology 188, 193–215.

Chang, L., Howie, R., Zussman, J., 1998. Non-silicates; sulphates, carbonates, phosphates, halides. Rock-Forming Minerals. The Geological Society of America, London. 378 pp.

Cherniak, D.J., Watson, E.B., Grove, M., Harrison, T.M., 2004. Pb diffusion in monazite: a combined RBS/SIMS study. Geochimica et Cosmochimica Acta 68, 829–840.

Corrie, S.L., Kohn, M.J., 2007. Resolving the timing of orogenesis in the Western Blue Ridge, southern Appalachians, via in situ ID-TIMS monazite geochronology. Geology 35 (7), 627–630.

Deuser, W.G., Herzog, L.F., 1962. Rubidium-strontium age determinations of muscovites and biotites from pegmatites of the Blue Ridge and Piedmont. Journal of Geophysical Research 67, 1997–2004.

Dumond, G., McLean, N., Williams, M.L., Jercinovic, M.J., Bowring, S.A., 2008. High-resolution dating of granite petrogenesis and deformation in a lower crustal shear zone: athabasca granulite terrane, western Canadian Shield. Chemical Geology 254, 175–196.

Fletcher, I.R., McNaughton, N.J., Davis, W.J., Rasmussen, B., 2010. Matrix effects and calibration limitations in ion probe U–Pb and Th–Pb dating of monazite. Chemical Geology 270 (1–4), 31–44.

Foster, G., Parrish, R.R., Horstwood, M.S.A., Chenery, S., Pyle, J., Gibson, H.D., 2004. The generation of prograde P-T-t points and paths; a textural, compositional, and chronological study of metamorphic monazite. Earth and Planetary Science Letters 228, 303–312.

Gehrels, G.E., Valencia, V.A., Ruiz, J., 2008. Enhanced precision, accuracy, efficiency, and spatial resolution of U–Pb ages by laser ablation-multicollector-inductively coupled plasma-mass spectrometry. Geochemistry, Geophysics, Geosystems 9 (3).

Harrison, T.M., McKeegan, K.D., Le Fort, P., 1995. Detection of inherited monazite in the Manaslu leucogranite by $^{208}Pb/^{232}Th$ ion microprobe dating. Earth and Planetary Science Letters 133, 271–282.

Harrison, T.M., Grove, M., McKeegan, K.D., Coath, C.D., Lovera, O.M., Le Fort, P., 1999. Origin and episodic emplacement of the Manaslu intrusive complex. Journal of Petrology 40, 3–19.

Hirata, T., Nesbitt, R.W., 1995. U–Pb isotope geochronology of zircon: evaluation of the laser probe-inductively coupled plasma mass spectrometry technique. Geochimica et Cosmochimica Acta 59, 2491–2500.

Horn, I., Rudnick, R.L., McDonough, W.F., 2000. Precise elemental and isotope ratio determination by simultaneous solution nebulization and laser ablation-ICP-MS: application to U–Pb geochronology. Chemical Geology 164, 281–301.

Horstwood, M.S.A., 2008. Data reduction strategies, uncertainty assessment and resolution of LA-(MC-)ICP-MS isotope data. In: Sylvester, P. (Ed.), Laser ablation ICP-MS in the Earth Sciences: current practices and outstanding issues: Mineralogical Association of Canada Short Course Series Volume, pp. 283–300.

Ireland, T.R., 1995. Ion microprobe mass spectrometry: techniques and applications in cosmochemistry, geochemistry, and geochronology. Advances in Analytical Geochemistry 2, 1–118.

Janots, E., Negro, F., Brunet, F., Goffé, B., Engi, M., Bouybaouene, M.L., 2006. Evolution of the REE mineralogy in HP–LT metapelites of the Sebtide complex, Rif, Morocco: monazite stability and geochronology. Lithos 87, 214–234.

Janots, E., Engi, M., Rubatto, D., Berger, A., Gregory, C., Rahn, M., 2009. Metamorphic rates in collisional orogeny from in situ allanite and monazite dating. Geology 37, 11–14.

Jercinovic, M.J., Williams, M.L., Lane, E.D., 2008. In-situ trace element analysis of monazite and other fine-grained accessory minerals by EPMA. Chemical Geology 254, 197–215.

Kohn, M.J., Malloy, M.A., 2004. Formation of monazite via prograde metamorphic reactions among common silicates: implications for age determinations. Geochimica et Cosmochimica Acta 68, 101–113.

Kohn, M.J., Vervoort, J.D., 2008. U–Th–Pb dating of monazite by single-collector ICP-MS; pitfalls and potential. Geochemistry, Geophysics, Geosystems 9 (4).

Kosler, J., Tubrett, M.N., Sylvester, P.J., 2001. Application of laser ablation ICP-MS to U–Th–Pb dating of monazite. Geostandards Newsletter 25, 375–386.

Krogh, T.E., 1973. A low contamination method for the hydrothermal decomposition of zircon and extraction of U and Pb for isotopic age determinations. Geochimica et Cosmochimica Acta 37, 485–494.

Krogh, T.E., 1982. Improved accuracy of U–Pb zircon ages by the creation of more concordant systems using an air abrasion technique. Geochimica et Cosmochimica Acta 46, 637–649.

Ludwig, K., 2003. Isoplot 3.00. Berkeley Geochronology Center Special Publication, 4. 70 pp.

Mattinson, J.M., 1987. U–Pb ages of zircons: a basic examination of error propagation. Chemical Geology 66, 151–162.
Mattinson, J.M., 2003. CA (Chemical Abrasion)-TIMS: high-resolution U–Pb geochronology combining high-temperature annealing of radiation damage and multi-step partial dissolution analysis. Eos, Transactions American Geophysical Union 84 Abstract V22E-06.
Mattinson, J.M., 2005. Zircon U–Pb chemical abrasion ("CA-TIMS") method: combined annealing and multi-step partial dissolution analysis for improved precision and accuracy of zircon ages. Chemical Geology 220, 47–66.
Meldrum, A., Boatner, L.A., Weber, W.J., Ewing, R.C., 1998. Radiation damage in zircon and monazite. Geochimica et Cosmochimica Acta 62 (14), 2509–2520.
Mundil, R., Ludwig, K., Metcalfe, I., Renne, P., 2004. Age and timing of the Permian Mass Extinctions: U/Pb dating of closed system zircons. Science 305, 1760–1763.
Nasdala, L., Lengauer, C.L., Hanchar, J.K., Kronz, A., Wirth, R., Blanc, P., Kennedy, A.K., Seydoux-Guillaume, A.M., 2002. Annealing radiation damage and the recovery of cathodoluminescence. Chemical Geology 191, 121–140.
Overstreet, W.C., 1967. The geologic occurrence of monazite. U.S. Geological Survey Professional Paper 530, 1–327.
Parrish, R.R., 1990. U–Pb dating of monazite and its application to geological problems. Canadian Journal of Earth Sciences 27, 1431–1450.
Peterman, E.M., Hacker, B.R., Grove, M., Gehrels, G.E., Mattinson, J.M., 2006. A multi-method approach to improving monazite geochronology. Eos, Transactions American Geophysical Union. TIMS, LA-ICP-MS, SIMS and EPMA.
Pyle, J.M., Spear, F.S., 1999. Yttrium zoning in garnet: coupling of major and accessory phases during metamorphic reactions. Geological Materials Research 1, 1–49.
Pyle, J.M., Spear, F.S., Rudnick, R.L., McDonough, W.F., 2001. Monazite-xenotime and monazite-garnet equilibrium in a prograde pelite sequence. Journal of Petrology 42, 2083–2117.
Pyle, J.M., Spear, F.S., Wark, D.A., 2002. Electron microprobe analysis of phosphates: pitfalls and protocols. Reviews in Mineralogy and Geochemistry 48, 337–362.
Rioux, M., Hacker, B.R., Mattinson, J., Kelemen, P., Blusztajn, J., Gehrels, G., 2007. The magmatic development of an intra-oceanic crustal section: high-precision U–Pb zircon and whole rock isotopic analyses from the accreted Talkeetna arc, south-central Alaska. GSA Bulletin 119, 1168–1184.
Schärer, U., 1984. The effect of initial ^{230}Th disequilibrium on young U–Pb ages: the Makalu case, Himalaya. Earth and Planetary Science Letters 67, 191–204.
Schärer, U., Allègre, C.J., 1982. Uranium–lead system in fragments of a single zircon grain. Nature 295, 585–587.
Seydoux-Guillaume, A.M., Wirth, R., Nasdala, L., Gottschalk, M., Montel, J.M., Heinrich, W., 2002a. XRD, TEM and Raman study of experimental annealing of natural monazite. Physics and Chemistry of Minerals 29, 240–253.
Seydoux-Guillaume, A.M., Paquette, J.-L., Wiedenbeck, Montel, J.-M., Heinrich, W., 2002b. Experimental resetting of the U–Th–Pb systems in monazite. Chemical Geology 191, 165–181.
Shakel, D.W., Silver, L.T., Damon, P.E., 1977. Observations on the history of the gneissic core complex, Santa Catalina Mountains, southern Arizona. Geological Society of America Abstracts with Programs 9, 1169–1170.
Spear, F.S., Pyle, J.M., Cherniak, D.J., 2009. Limitations of chemical dating of monazite. Chemical Geology 266, 218–230.
Stacey, J.S., Kramers, J.D., 1975. Approximation of terrestrial lead isotope evolution by a two-stage model. Earth and Planetary Science Letters 26, 207–221.
Stern, R.A., Berman, R.G., 2001. Monazite U–Pb and Th–Pb geochronology by ion microprobe with an application to in situ dating of an Archean metasedimentary rock. Chemical Geology 172, 113–130.
Suzuki, K., Adachi, M., 1991. Precambrian provenance and Silurian metamorphism of the Tsunosawa paragneiss in the south Kitami terrane, northeast Japan, revealed by chemical Th–U–total Pb isochron ages of monazite, zircon and xenotime. Geochemical Journal 25, 357–376.
Wetherill, G.W., 1956. Discordant uranium-lead ages Trans. Am. Geophys. Union 37, 320–326.
Williams, M.L., Jercinovic, M.J., Terry, M.P., 2002. Microprobe monazite geochronology: putting absolute time into microstructural analysis. Journal of Structural Geology 24, 1013–1028.
Williams, M.L., Jercinovic, M.J., Hetherington, C.J., 2007. Microprobe monazite geochronology: understanding geologic processes by integrating composition and chronology. Annual Review of Earth and Planetary Sciences 35, 137–175.